Implications of using spheroidal "cone model" CMEs in solar-wind models

Owens, M. J. ORCID: https://orcid.org/0000-0003-2061-2453, Barnard, L. A. ORCID: https://orcid.org/0000-0001-9876-4612, Verbeke, C. ORCID: https://orcid.org/0000-0002-9402-5609, McGinness, B. P. S., Turner, H. ORCID: https://orcid.org/0000-0002-4012-8004, Chi, Y. ORCID: https://orcid.org/0000-0001-9315-4487, Gyeltshen, D. ORCID: https://orcid.org/0009-0004-8411-7042 and Lockwood, M. ORCID: https://orcid.org/0000-0002-7397-2172 (2025) Implications of using spheroidal "cone model" CMEs in solar-wind models. Space Weather, 23 (6). e2025SW004397. ISSN 1542-7390 doi: 10.1029/2025SW004397 Available at https://centaur.reading.ac.uk/123032/

www.reading.ac.uk/centaur

CentAUR

Central Archive at the University of Reading

Reading's research outputs online

Implications of Using Spheroidal "Cone Model" CMEs in Solar-Wind Models

M. J. Owens[1] , L. A. Barnard[1] , C. Verbeke[2,3] , B. P. S. McGinness[1], H. Turner[1] , Y. Chi[4] , D. Gyeltshen[1] , and M. Lockwood[1]

[1]Department of Meteorology, University of Reading, Reading, UK, [2]Heliophysics Science Division, NASA Goddard Space Flight Center, Greenbelt, MD, USA, [3]Centre for mathematical Plasma Astrophysics (CmPA), KU Leuven, Leuven, Belgium, [4]Deep Space Exploration Laboratory, Institute of Deep Space Sciences, Hefei, China

Abstract Space-weather forecasting requires advanced prediction of the arrival time and properties of coronal mass ejections (CMEs) in near-Earth space. Kinematic properties of CMEs close to the Sun—such as speed, direction and angular width—are routinely estimated from coronagraph images by using three-dimensional geometric models, such as the "cone model." These are used to characterize a time-dependent perturbation at the inner boundary of a numerical solar-wind model, normally at 0.1 AU, enabling a forecast of the CME arrival time and speed at Earth. This perturbation is typically spheroidal in shape. In this study we show that spheroidal CMEs exhibit four features inconsistent with observations that may limit the accuracy of space-weather forecasts: 1, Slow spheroidal CMEs intersect the model inner boundary for a long duration and hence resist acceleration by the ambient solar wind, producing longer transit times than observed; 2, The radial extent of a spheroidal CME is directly related to its angular width. Observations of CMEs at 1 AU do not display any relation between angular width and radial extent; 3, Fast-and-wide CMEs cannot be sufficiently decelerated by the ambient solar wind and arrive with higher speeds than observed; 4, Spheroidal CMEs show different magnitudes of interplanetary accelerations for different angular widths, contrary to observations. We show that fixing the CME duration at the inner boundary—which mimics observed CME expansion—alleviates these problems. The choice of fixed duration is a free parameter that needs to be calibrated against observations, but 8 hr works reasonably well.

Plain Language Summary Severe space weather can damage ground- and space-based technologies. It results from changing conditions in the Sun's magnetic field, which drives large-scale eruptions from the Sun's atmosphere that travel out through the solar system. If such eruptions, called coronal mass ejections (CMEs), are directed toward Earth they can potentially disrupt satellites, GPS and power grids. Consequently, it is desirable to forecast if and when a CME will arrive at Earth. For the last 20 years, CMEs have been treated as spherical structures in computer simulations used to routinely forecast space weather. We perform experiments using a computer simulation of the solar wind to show that treating CMEs as spheres produces a number of features that are inconsistent with observations. In particular, the angular width of spherical CMEs affects how easily the solar wind can slow them down, and hence the time it takes for CMEs to reach Earth. But this trend is not observed. We suggest a simple alternative approach to spherical CMEs that mimics the observed expansion of CMEs and behaves closer to the available observations. This will enable space weather to be forecast more accurately in the future.

1. Introduction

Direct observations of the solar-wind conditions at the first Lagrange point (L1), just upstream of Earth, can be used as the basis of accurate space-weather forecasts. However, the proximity of L1 to Earth means that forecast lead times are limited to less than an hour. As the solar wind is a supersonic, approximately radial outflow, extending forecast lead times beyond an hour requires initializing forecasts using information about the solar-wind flow closer to the Sun. There now exists capability to simulate both the solar wind and coronal mass ejections (CMEs), from initiation in the corona through to arrival in near-Earth space, using high-resolution, detailed physic-based numerical models (e.g., Jin et al., 2017; Lynch et al., 2025; Torok et al., 2018). But this approach is not feasible for operational space-weather forecasting, due a lack of adequate real-time observations with which to initialize such simulations, the high computational expense and the long simulation run time.

Instead, long lead-time operational forecasting necessitates a more pragmatic approach. It currently uses a three-step process:

1. Near-Sun ambient solar-wind conditions, typically at 0.1 AU, are estimated using coronal models, themselves constrained by the observed photospheric magnetic field (e.g., Arge et al., 2003; Riley et al., 2001; van der Holst et al., 2014).
2. Near-Sun CME properties are estimated by fitting a simple geometric model to white-light coronagraph observations (Michalek et al., 2003; Thernisien et al., 2009; Zhao et al., 2002).
3. Coronal model output is used as the inner boundary conditions for a solar wind model from 0.1 to beyond 1 AU (e.g., Merkin et al., 2016; Owens, Lang, et al., 2020; Pomoell & Poedts, 2018; Riley et al., 2001; Toth et al., 2005). Suitable time-dependent perturbations are also added at solar-wind model inner boundary to mimic observed CMEs (Emmons et al., 2013; Lee et al., 2015; Mays et al., 2015; Odstrcil, Riley, & Zhao, 2004; Scolini et al., 2018).

Whilst the coronal and solar-wind models have changed or been improved, this same general methodology has been used for more than 20 years (e.g., Odstrcil, Riley, & Zhao, 2004; Riley et al., 2018). Indeed, all of the operational space-weather forecast centers currently rely on this approach. This study focuses on how the coronagraph-derived CME properties (step 2) are implemented in the solar-wind models (step 3).

Coronagraph images (e.g., Brueckner et al., 1995) of CMEs are interpreted using geometric models, often referred to as "cone models" due to the simple shape employed. More complex geometries are also used (Thernisien et al., 2009; Zhao et al., 2002), but the general implications discussed here are the same. These geometric models all aim to determine the true three-dimensional properties of the CME from the two-dimensional projections in coronagraph images. Typically, this results in estimates of the radial speed, direction and angular extent of the CME with respect to the Sun. In order to represent such a transient CME structure within a solar-wind model, a speed perturbation with the same general properties is introduced at the model inner boundary, sometimes with an associated change in the plasma parameters (Odstrcil, Pizzo, et al., 2004).

By far the most common implementation of cone-model CMEs in solar-wind models is to approximate the CME as a spherical perturbation which advects through the solar-wind model inner boundary. For this purpose, the solar-wind model inner boundary is often approximated as planar—rather than spherical—to simplify geometry. This slightly distorts the CME from a pure spherical shape. Non-spherical implementations of the cone-model CMEs can also be constructed by design. For example, the CME can present a non-circular cross-section at the inner boundary (Scolini & Palmerio, 2024), which may better match the flux-rope structure implied by the more sophisticated geometric models (Thernisien et al., 2009). While this does have an effect on resulting CME dynamics for "glancing blows"—where the point of encounter with the CME is far from the center of the CME—it does not significantly affect the speed and transit time for the center of the CME (Scolini et al., 2018). We refer to all these approaches as "spheroidal CMEs."

Three commonly used methods for translating from coronagraph-derived cone-CME parameters to spheroidal CME perturbations are shown schematically in Figure 1. In each case, the solar-wind model has an inner boundary at a heliocentric distance of r_{IN}, and a cone-model CME has angular half-width α. Panel (a) shows a widely used implementation where the radius of the spheroidal perturbation, r_0, is approximated as $r_{IN} \tan \alpha$ (Pomoell & Poedts, 2018; Scolini et al., 2018). The issue with this approximation is that the perturbation will have an angular width greater than the cone-model estimate. Panel (b) shows a slight modification, wherein $r_0 = r_{IN} \sin \alpha$ (e.g., Zhao et al., 2002). This produces smaller CMEs than the $\tan \alpha$ method, preserving the original α value and producing a smaller r_0. A third approach, shown in panel c, is to prescribe the CME as a spherocylinder; essentially a short, fat sausage. Assuming the spherical portion is described by $r_0 = r_{IN} \sin \alpha$, this method also preserves the cone-model α, but allows for "thicker" radial extents, which can be desirable for reasons explained below. All these approaches still determine the radial extent of the CME perturbation solely based on the CME angular width. that is, For all spheroidal CMEs, r_0 is some function of α.

This relation is important to CME dynamics, as it controls the duration of the perturbation pulse (Δt) inserted at the solar-wind model inner boundary. As demonstrated in Section 2, Δt is broadly analogous to the total initial momentum of the CME, as it determines the extent to which a CME accelerates or decelerates toward the ambient solar wind during its propagation to 1 AU.
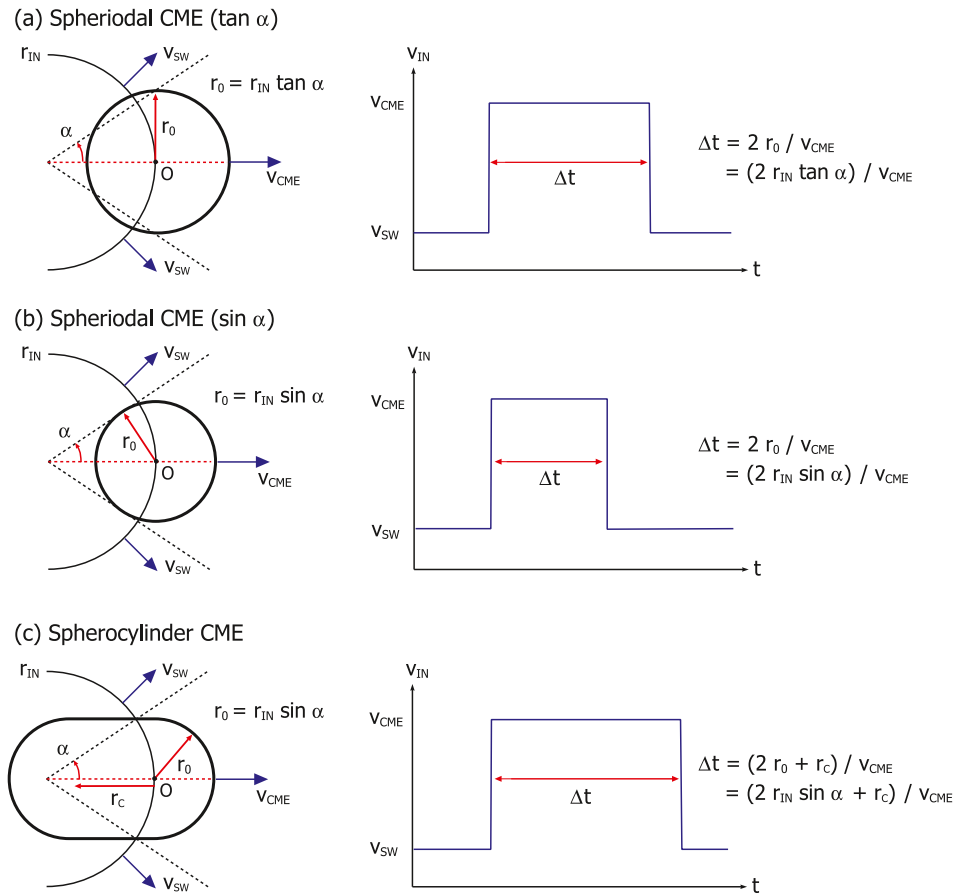
Figure 1. Schematics of different spheroidal coronal mass ejection (CME) implementations. Left: A view of the solar equatorial plane. The spheroidal CME boundary is shown by the thick black line. (a) A spheroidal CME where the initial radius, r_0, is approximated as $r_{IN} \tan \alpha$, where r_{IN} is the heliocentric radius of the solar-wind model inner boundary and α is the cone-model CME angular half-width. (b) A spheroidal CME where the initial radius, r_0, is approximated as $r_{IN} \sin \alpha$. (c) A spherocylinder CME where the initial radius, r_0, is approximated as $r_{IN} \sin \alpha$ and the cylinder has length r_C. Right: The solar wind time series at the point O on the solar-wind inner boundary. The CME threads the inner boundary for a time Δt, during which the speed is set to the CME speed, that is, $V_{in} = V_{CME}$. At other times, the speed is the ambient solar wind speed, that is, $V_{IN} = V_{SW}$.

A spheroidal CME advects through the solar-wind model inner boundary at the radial speed of the CME estimated from a cone model, V_{CME}. Thus for a given V_{CME}, Δt increases linearly with r_0, and hence non-linearly with α. For case (a) in Figure 1, this relation will be $\Delta t = (2r_{IN} \tan \alpha)/V_{CME}$, for case (b) $\Delta t = (2r_{IN} \tan \alpha)/V_{CME}$, and for case (c) $\Delta t = (2r_{IN} \sin \alpha + r_C)/V_{CME}$, where r_C is the length of the cylindrical section of the spherocylinder. Thus in all cases, Δt will be inversely proportional to V_{CME}. Of course, the curved nature of the CME front means that the radial extent of the CME, and hence Δt for a given point of encounter, will decrease with angle from the nose of the CME (this decrease is smaller for the spherocylinder, which has a constant contribution to the total radial extent at all locations due to the cylindrical portion). But for simplicity, we here limit consideration to the "direct hit" CMEs, where the radial extent of the CME perturbation is maximum.

This study examines the implications of this spherical perturbation approach to CME propagation and hence operational space-weather forecasting. Section 2 introduces the HUXt solar-wind model that will be used to investigate CME propagation and uses HUXt to illustrate the current method used in operational forecasting and the implications for CME dynamics in the heliosphere. Section 3.1 outlines a set of CMEs observed both near the Sun and in near-Earth space. Section 3.2 examines the relations between CME speed, angular width and transit time for the observed data set and for spheroidal CMEs in the HUXt model. We also propose and test a simple alternative implementation of cone-model CMEs in solar-wind models, based on fixing Δt. This is equivalent to

the radial extent being proportional to CME speed, mimicking CME expansion. Section 4 discusses the implications of the results and future avenues for improving forecasting.

2. The HUXt Solar Wind Model

In order to investigate CME propagation from the Sun to Earth, we use the Heliospheric Upwind eXtrapolation with time dependence (HUXt) solar-wind model (Barnard & Owens, 2022; Owens, Lang, et al., 2020). HUXt is a dynamical model that approximates the solar wind as a 1-dimensional, incompressible, hydrodynamic flow (see also Riley & Lionello, 2011). Thus, solar-wind flows accelerate and decelerate through stream interaction, but only solar-wind radial speed (not density or temperature) is simulated. Despite these gross approximations, HUXt produces solar-wind speeds throughout the model domain from 0.1 to 1 AU that agree very closely with 3-dimensional magnetohydrodynamic model results for the same boundary conditions (Owens, Lang, et al., 2020), but at a fraction of the computational cost. Given the relatively large parameter space that needs to be investigated in this study, the computational efficiency of HUXt is desirable. But as HUXt and 3D MHD models produce similar CME dynamics for the same boundary conditions, the results presented here are expected to be generally applicable to a wide range of solar-wind models when employing the cone model CME approximation (i.e., when CMEs are treated as speed and/or density, temperature perturbations).

To illustrate the relations between V_{CME}, α and Δt, some examples of spheroidal CMEs are shown using the HUXt model in Figures 2a and 2c. The spheroidal CMEs are speed perturbations inserted into a uniform solar wind of speed 300 km s^{-1} at the model inner boundary at 0.1 AU. The boundaries of the inserted CME speed perturbations, shown as colored lines, are tracked using passive tracer partices (see Barnard & Owens, 2022, for more detail).

In Figure 2a, four spheroidal CMEs (using the $\sin \alpha$ approximation) have been inserted at the same time, with the same launch speed of $V_{CME} = 600$ km s^{-1}, but with a range of α values. After 3.35 days, the wider CMEs—with $\alpha = 45$ and $60°$—have passed 1 AU, whereas the narrower CMEs—with $\alpha = 15$ and $30°$—are still inside 1 AU. Thus, for spheroidal CMEs, there is a relation between angular width and transit time to 1 AU, as expected. As will be shown later, there is no observational evidence to support this (faster CMEs generally are wider, but they do not appear to transit any faster or slower than their initial speed alone suggests).

Figure 2c shows α fixed at $60°$ for a range of V_{CME}. The snapshot is shown 3.05 days after launch. For lower launch speeds ($V_{CME} < 1200$ km s^{-1}), the basic trend is as expected: higher V_{CME} results in the CME traveling further in a given time. However, the $V_{CME} = 1200$ and 2,400 km s^{-1} CMEs are both at approximately 1 AU after 3.05 days. The reason for this is apparent; the faster initial speed means the CME moves through the inner boundary of the model in a shorter time. For the 2,400 km s^{-1} CME, the high speed, narrow angular extent and the spherical approximation combine to produce a speed perturbation at the inner boundary that is less than 2 hr in duration. This low Δt reduces the CME's ability to withstand deceleration by the slower ambient solar wind, despite the higher V_{CME}. The spheroidal CME approach also results in the radial extent of the CME at 1 AU being inversely proportional to the speed of the CME. Again, as shown below, there is no observational support for either of these relations.

3. Results

3.1. Observed CMEs

In order to quantify the observed trends between CME speeds, angular widths, radial extents and transit times to 1 AU, we begin with the updated Richardson and Cane (2010) list of human-identified interplanetary CMEs (ICMEs) in near-Earth space, which spans 1996 to 2024. The updated version is available at https://izw1.caltech.edu/ACE/ASC/DATA/level3/icmetable2.htm. Of the approximately 600 ICMEs in the list, 94 have been uniquely associated with near-Sun observations of an Earth-directed CME in the DONKI database (https://ccmc.gsfc.nasa.gov/tools/DONKI/). The cone-CME parameters provided in DONKI are primarily from the Moon-to-Mars (M2M) Space Weather Analysis Office, from (human) analysis of available coronagraph data. We cross-referenced these 94 events in the two catalogs, but were only able to identify DONKI CMEs within 2 hr of the times listed in the Richardson and Cane (2010) catalog for 84 events (it is possible the DONKI events have been updated by subsequent analysis). This list of 84 CME-ICME associations is used in the remainder of the study and is provided as Supporting Information S1. The lack of internal magnetic field in cone CMEs means that
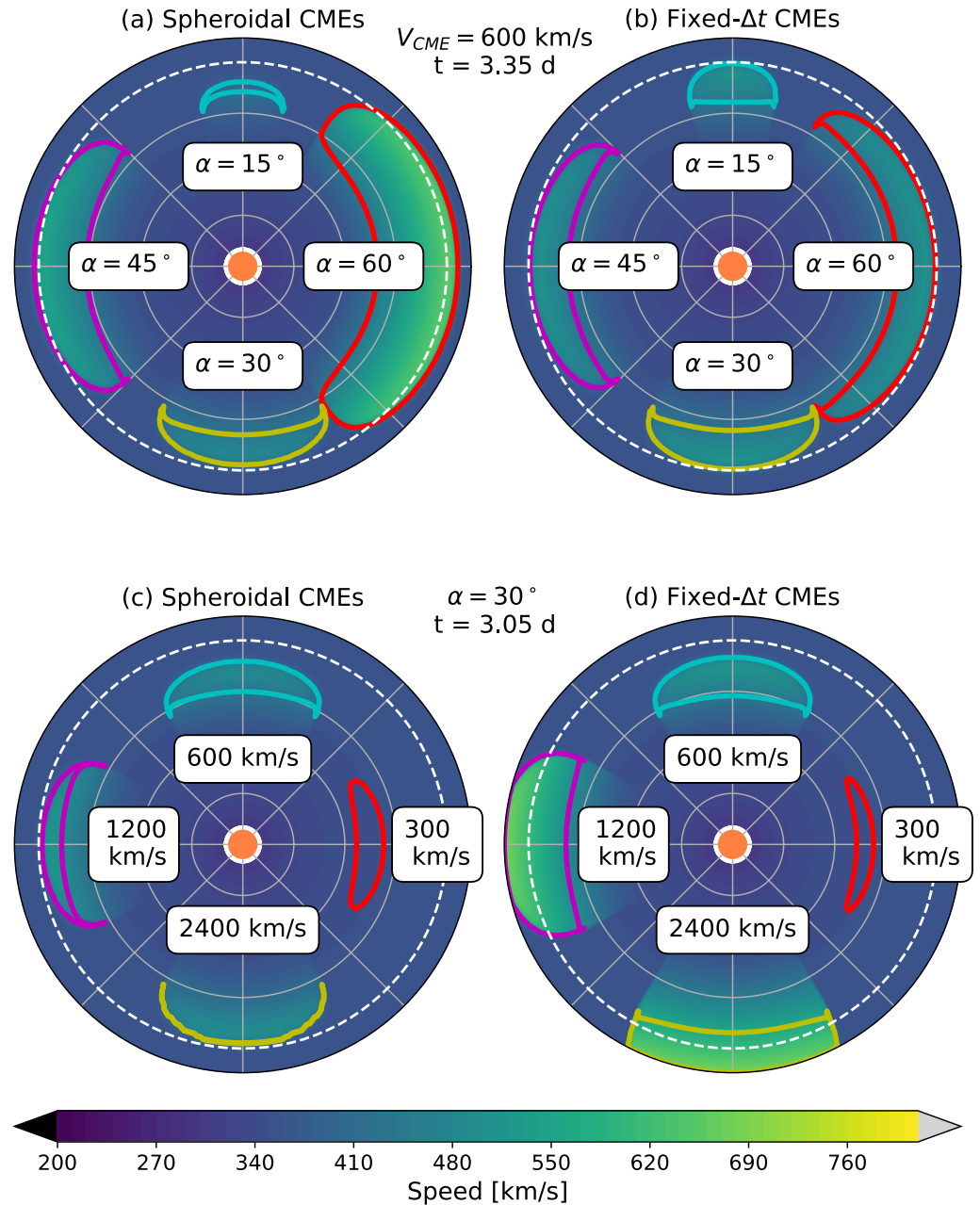
Figure 2. The solar equatorial plane from 0.1 to 1.1 AU from the HUXt model, for a uniform ambient solar wind of initial speed 300 km/s. 1 AU is shown as the white dashed circle. CMEs have been inserted at identical launch times. In the top panels (a, b), all CMEs have initial speeds $V_{CME} = 600$ km s^{-1} and varying CME angular half-widths, α, as labeled. The snapshot is shown 3.35 days after CME launch. In the bottom panels (c and d), all CMEs have $\alpha = 30°$ and a range of V_{CME} values, as labeled. Left-hand panels (a, b) show spheroidal CMEs, where the pulse duration, Δt varies as $\Delta t = (\tan \alpha)/(V_{CME})$. Right-hand panels (b, d) show CMEs with fixed $\Delta t = 8$ hrs, irrespective of V_{CME} and α.

solar wind models do not resolve ICME substructure, such as the shock, sheath and ICME leading and trailing edges. The ICME arrival time at 1 AU is therefore taken to be the time of the leading solar wind disturbance in both the model and in situ solar wind observations.

Figure 3 shows a summary of the properties of the 84 observed CME-ICME associations. Panel (a) shows that there is a reasonable correlation between the CME radial speed at 0.1 AU, V_{CME}, and CME angular half-width, α, as estimated by cone model fits to coronagraph observations. The linear correlation coefficient, r_L, is 0.61. For 84
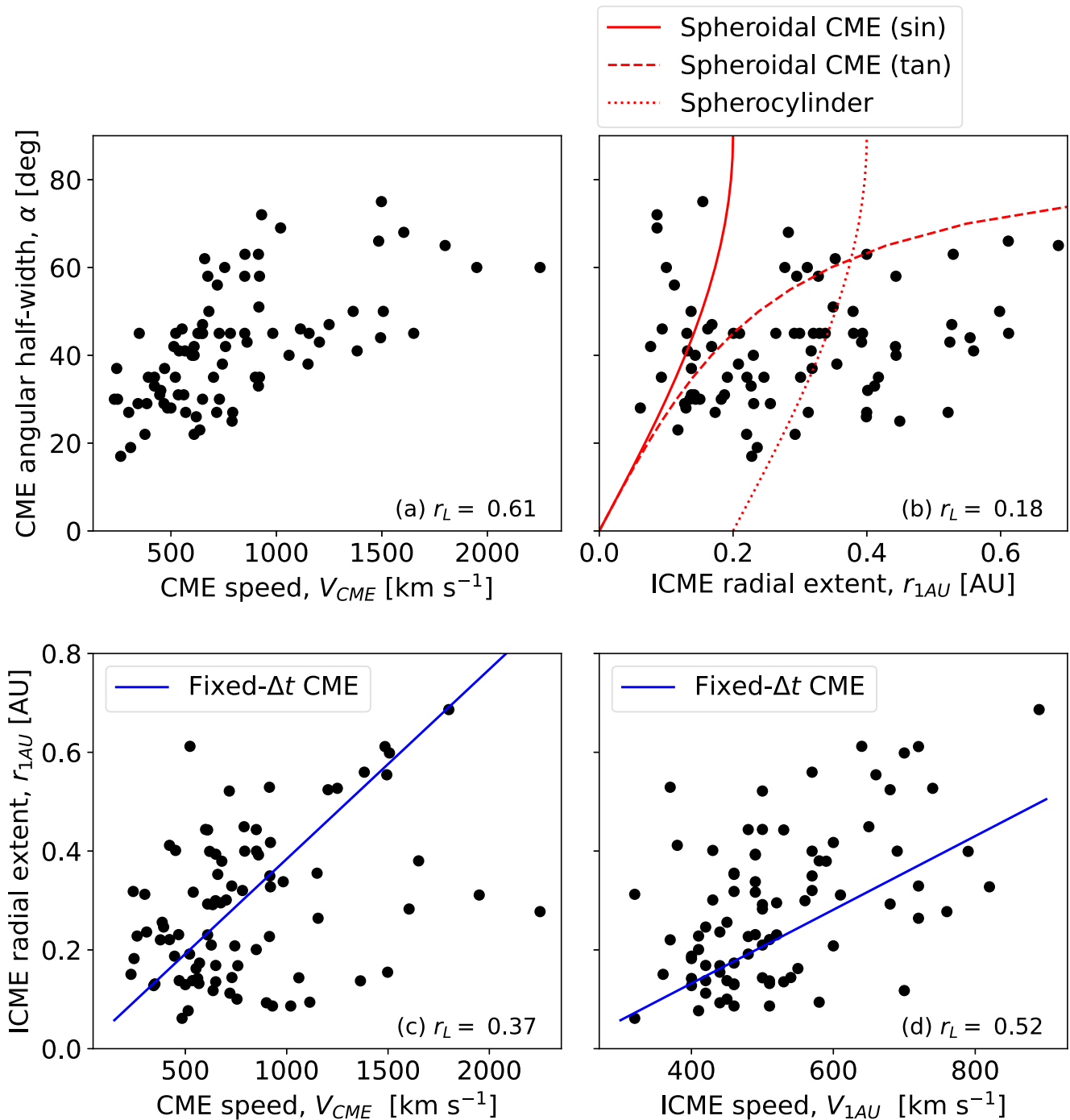
Figure 3. A summary of observed properties of CMEs near the Sun and the resulting ICMEs at Earth. (a) CME angular half-width, α, as a function of CME radial speed at 0.1 AU, V_{CME}. Both parameters are determined from cone model fits to coronagraph observations. (b) α as a function of the ICME radial extent at 1 AU, r_{1AU}, estimated as the product of the ICME duration and average ICME radial speed. (c) r_{1AU} as a function of V_{CME}. (d) r_{1AU} as a function of maximum ICME speed, V_{1AU}. Panel text shows the linear correlation coefficients, r_L for each set of relations. The red lines in panel b show the spheroidal CME relations between α and radial extent at 0.1 AU. Blue lines in panels (c, d) show the expected relations between speed and CME radial extent at 0.1 AU for fixed-Δt CMEs.

independent data points, this value is significantly different from zero correlation at the 99% confidence level. Panel (b) shows α as a function of ICME radial extent at 1 AU, r_{1AU}. This is estimated as the product of the ICME duration—computed from the ICME start and end times in the Richardson and Cane (2010) catalog—and the average ICME radial solar wind speed (Temmer et al., 2021). As ICMEs are often still expanding as they pass 1

Figure 4. A summary of coronal mass ejection (CME) kinematics for the 84 events from combined coronagraph and in situ observations. Blue dots show CMEs with coronagraph estimates of $\alpha < 35°$, black shows $35° \leq \alpha < 55°$, and red shows $\alpha \geq 55°$. Panel a shows the 0.1 to 1-AU transit time, τ, as a function of CME radial speed at 0.1 AU, V_{CME}. Panel (b) shows 1-AU ICME speed, V_{1AU}, 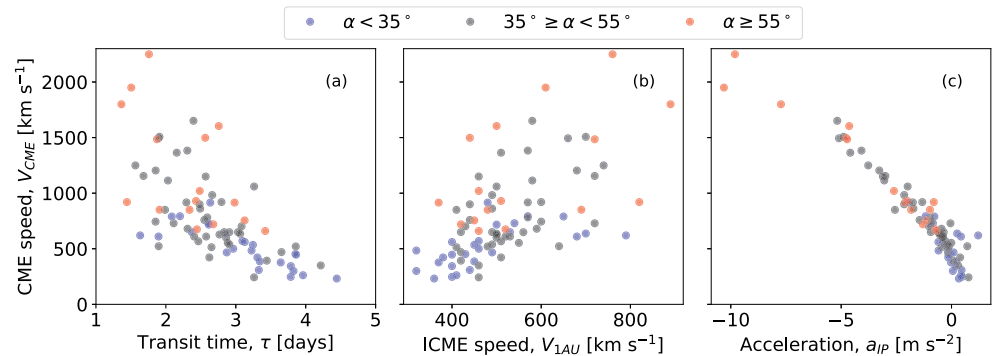as a function of V_{CME}. Panel (c) shows a_{IP}, the average acceleration between the 0.1 and 1 AU, as a function of V_{CME}. While wider CMEs are generally faster, the relations between CME speed and subsequent kinematic properties do not seem to be further ordered by α.

AU, this method of estimating r_{1AU} likely presents an upper limit. But here we only consider the trends in r_{1AU}, not the absolute values. There is very little correlation between α and r_{1AU} ($r_L = 0.18$, which is not statistically significantly different from 0, even at the 90% confidence level). The red lines show the spheroidal-CME relations between CME radial extent at 0.1 AU and α. Note that the observed relation is for r_{1AU}, not radial extent 0.1 AU. However, the lack of expected trend in the observations suggests that the spheroidal CME approximation may not be valid. It should be noted that these events are a mix of nose and flank encounters of the ICME at 1 AU. This will introduce noise into any relations between speed, angular width and radial extent. But it is not expected to have any systematic effects on those trends.

Figures 3c and 3d show the relation of r_{1AU} with V_{CME} and maximum ICME speed, V_{1AU}, respectively. There are weak but significant correlations present ($r_L = 0.37$ and 0.52, respectively, which are both significantly different from zero correlation at the 99% confidence level). This is consistent with faster ICMEs expanding more in the radial direction (Owens et al., 2005). This is contrary to the implicit assumption of spheroidal CMEs, which exhibit no relation between CME radial extent at 0.1 AU and CME speed. It is not possible to draw strong conclusions, however, as the observations are for r_{1AU}, not radial extent at 0.1 AU, and interplanetary dynamics and expansion will contribute to r_{1AU}.

Figure 4a shows the observed 0.1 to 1 AU transit time, τ, as a function of V_{CME} for the 84 CME-ICME associations. The observed τ values span approximately 1.5–4.5 days. There is a general trend toward lower τ for higher V_{CME}, but there is a good deal of scatter. This scatter is expected for a number of reasons (e.g., Temmer et al., 2023). Firstly, there is uncertainty in V_{CME} estimated from fitting cone models to coronagraph observations, as well as deriving the time of the CME leading edge at 0.1 AU. Secondly, the CMEs have a range of different propagation angles with respect to the Earth-Sun line, meaning that not all ICMEs will be "direct hits", which can have significant impact on arrival times (e.g., Owens & Cargill, 2004; Scolini & Palmerio, 2024). Thirdly, the CMEs will have propagated into a range of different ambient solar wind conditions and possibly other CMEs, which has also been shown to influence CME propagation and transit time (e.g., Case et al., 2008; Temmer et al., 2023; Wu et al., 2024).

The colors in Figure 4a indicate different coronagraph-derived estimates of CME angular width, with blue dots showing CMEs with $\alpha < 35°$, black shows $35° \leq \alpha < 55°$, and red shows $\alpha \geq 55°$. The trend of faster CMEs having greater angular extent is apparent here. But for a given V_{CME}, there does not appear to be any systematic effect of α on τ.

Figure 4b shows that higher V_{CME} generally produces faster ICMEs at 1 AU, though again there is a great deal of scatter, for the same reasons as discussed above. Note that the 1-AU ICME speed, V_{1AU} is here taken to be the maximum ICME speed from Richardson and Cane (2010), as this generally represents the leading-edge speed (Owens et al., 2005). Again, α does not appear to order the observations beyond the trend with V_{CME}. The best-fit

linear trend (not shown) is given by $V_{1AU} = 0.15 V_{CME} + 397 \text{ km s}^{-1}$, consistent with the slowest CMEs being accelerated up to the ambient solar wind of approximately 400 km s^{-1}.

To better quantify the speed and transit time relations, Figure 4c shows the average interplanetary acceleration, a_{IP},

$$a_{IP} = \frac{V_{1AU} - V_{CME}}{\tau}, \qquad (1)$$

as a function of V_{CME}. As first described by Gopalswamy et al. (2000, 2001), there is a strong, approximately linear relation between a_{IP} and V_{CME}, with $a_{IP} = 0$ occurring around $V_{CME} = 350$ to 450 km s^{-1}. This is a typical ambient solar-wind speed, again suggesting CMEs moving slower than the ambient solar wind are accelerated, while those moving fast are decelerated. Such behavior is broadly consistent with a drag force acting on CMEs during propagation to 1 AU (Cargill, 2004; Vrsnak & Gopalswamy, 2002). The observed V_{CME}-a_{IP} relation appears to be the same regardless of CME angular width.

3.2. Modeled Spheroidal CMEs

We next look at the results of modeling CMEs as spheroidal perturbations with HUXt. In order to clearly isolate the effects of the spheroidal-CME approximation, we seek to simplify everything else about the model runs. HUXt is typically used with a realistically structured ambient solar wind provided by a coronal model. However, in this study we are not seeking to accurately model the propagation of individual CMEs, but to investigate trends in CME propagation which result from different approaches to "cone model" CMEs. Therefore a uniform ambient solar wind of initial speed 350 km s^{-1} at the inner boundary of 0.1 AU is used for all runs. Due to continued solar wind acceleration within the model domain, this results in ambient solar-wind speeds of approximately 400 km s^{-1} at 1 AU, which is fairly typical for slow wind.

We consider CMEs with α values at the center of the three bins used for the observations in Figure 4. that is, $\alpha = 25, 40$ and $65°$. For spherocylinder CMEs, we only consider $r_c = 0.2$ AU. This is a relatively large value, chosen to highlight the difference of this approach from $\sin \alpha$ spheroidal CMEs, which are effectively spherocylinder CMEs with $r_C = 0$. As will be seen below, it is also the value required in order to approximately match the transit times of the fastest CMEs.

Figure 5 shows that the different spheroidal CME approaches show qualitatively similar results in terms of CME kinematics. In Figure 5a it can be seen that for low V_{CME}, all forms of spheroidal CME produce anomalously long transit times (>5 days), regardless of α. This is because the low V_{CME} produces a very long Δt. Such a long CME pulse means the faster ambient wind inserted behind the pulse will not be able to catch up with the CME leading edge. Effectively, long Δt makes it more difficult to accelerate the CME to the ambient solar-wind speed than a shorter CME pulse.

This same effect can also be seen for faster CMEs with smaller radial extents (those are $\sin \alpha$ CMEs, and the $\tan \alpha$ CMEs with smaller angular extents. For these events, the ambient solar wind is too effective at slowing them and τ plateaus around $V_{CME} = 1000 \text{ km s}^{-1}$, resulting in an overestimate of τ compared with observed values. The increased Δt gained by the radial extent of wide $\tan \alpha$ CMEs and the spherocylinder CMEs does provide a reasonable match to the observed τ for the fastest CMEs.

Figures 5a and 5b show that while wide spherical CMEs do produce the low τ values that are observed for faster CMEs, this results in a large overestimate of the 1-AU speed of CMEs, V_{1AU}. This is because wide spherical CMEs produce long Δt regardless of V_{CME}, and thus do not decelerate sufficiently by 1 AU.

All spheroidal approaches show V_{1AU} reaching a maximum value around $V_{CME} = 1000 \text{ km s}^{-1}$, contrary to observations. In fact, there is a small decrease in V_{1AU} for the very highest values of V_{CME}. This is a numerical artifact; higher V_{CME} values produce both stronger V gradients and shorter pulses at the inner boundary, which are subject to increased numerical diffusion (despite being well below the Courant–Friedrichs–Lewy limit for numerical stability), leading to slower CME speeds at 1 AU. There is also a small hint of an increase in τ for high V_{CME}. Increasing the spatial and temporal resolution of the HUXt model alleviates this, causing V_{1AU} to plateau around $V_{CME} = 1000 \text{ km s}^{-1}$, rather than slightly decline. While this is trivial to implement in HUXt, as it is very
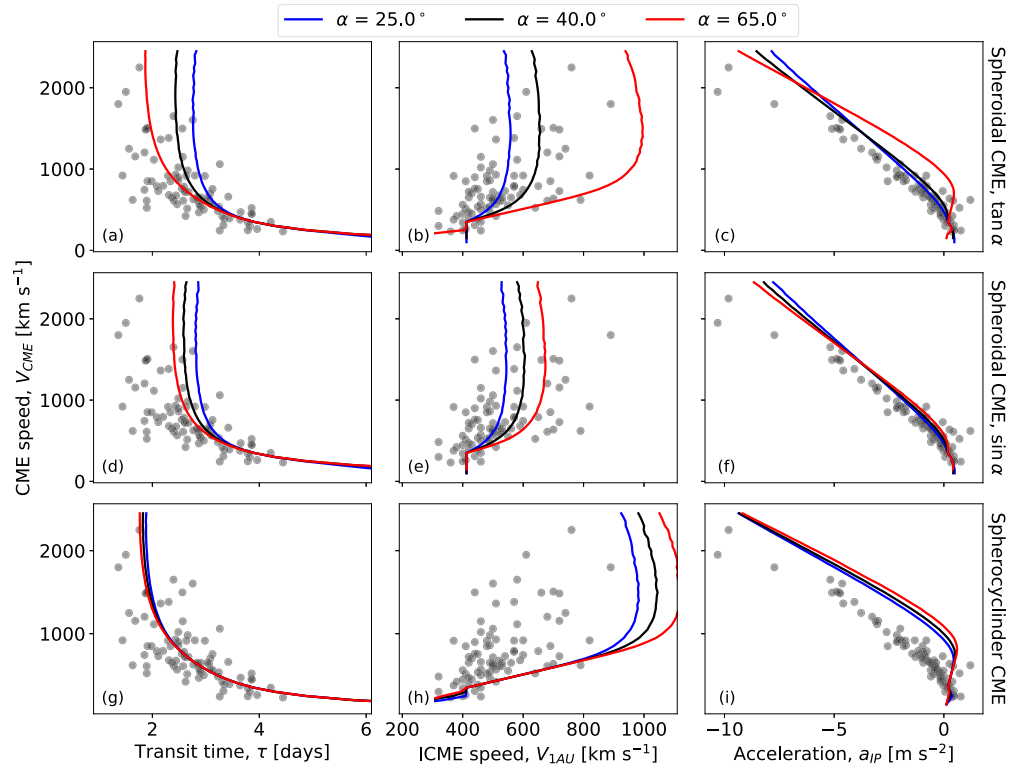
Figure 5. A summary of observed and modeled coronal mass ejection (CME) kinematics for spheroidal CMEs. Black dots show combined coronagraph and in situ observations. Lines in the top panels (a–c) show results from HUXt for spheroidal CMEs using $r_0 = \tan \alpha$ for a range of α (blue, black and red corresponding to $\alpha = 25, 40$ and $65°$, respectively). Middle panels (d–f) show the same for spheroidal CMEs using $r_0 = \sin \alpha$. Bottom panels (g–i) show the spherocylinder CME using $r_C = 0.2$ AU. Left-hand panels (a, d and g) show the 0.1 to 1-AU transit time, τ as a function of CME radial speed at 0.1 AU, V_{CME}. Middle panels (b, e and h) show 1-AU ICME speed, V_{1AU}, as a function of V_{CME}. Right-hand panels (c, f and i) show the average acceleration between 0.1 and 1 AU, a_{IP}, as a function of V_{CME}.

computationally efficient, we choose to show the lower resolution results here as greatly increasing resolution would be undesirable in more sophisticated three-dimensional MHD models, particularly in forecast scenarios. Even with increased computational resource, the modeled behavior (of constant V_{1AU} for $V_{CME} > 1000$ km s^{-1}) would remain, contrary to the observed trend.

The net effect of these behaviors are shown in the right-hand panels of Figure 5. The average interplanetary acceleration, a_{IP}, for wide $\tan \alpha$ spheroidal CMEs is markedly different from narrow and typical spheroidal CMEs. Wide $\tan \alpha$ spheroidal CMEs show a net positive acceleration for CMEs with $V_{CME} \leq 1000$ km s^{-1}, contrary to observations, and insufficient deceleration for CMEs with $V_{CME} > 1000$ km s^{-1}. For the $\sin \alpha$ spherical CMEs and spherocylinder CMEs, this α-dependence is much weaker.

Thus, more accurate estimates of τ can be achieved by using wide $\tan \alpha$ spheroidal CMEs (regardless of observed α) or "thick" spherocylinder CMEs. But that is offset by greatly overestimating V_{1AU} for slow and moderate speed CMEs, and producing interplanetary acceleration profiles which are not consistent with observations. This is problematic for two reasons. Firstly, prediction of V_{1AU} is itself important for space-weather forecasting (Owens, Lockwood & Barnard, 2020). Secondly, it suggests that even when a match can be produced for 1-AU arrival times, the location of the CME at other points in the heliosphere would be incorrect.

The $\sin \alpha$ CMEs are equivalent to spherocylinder CMEs with $r_C = 0$. As $\sin \alpha$ CMEs produce reasonable values at moderate CME speeds and spherocylinder CMEs with $r_C = 0.2$ AU produce reasonable values at high CME speeds, these results suggest that making r_C a constant value is not the best solution. It suggests that r_C needs to be a function of V_{CME}.
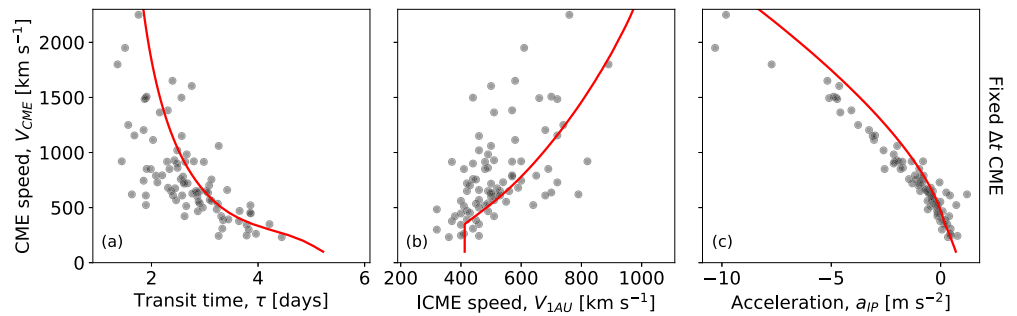
Figure 6. A summary of observed and modeled coronal mass ejection (CME) kinematics for fixed-Δt CMEs. Black dots show combined coronagraph and in situ observations. Red lines show results from HUXt for spheroidal CMEs with a fixed duration at 0.1 AU of 8 hr. Panel (a) shows the 0.1 to 1-AU transit time, τ, as a function of CME radial speed at 0.1 AU, V_{CME}. Panel (b) shows 1-AU ICME speed, V_{1AU}, as a function of V_{CME}. Panel (c) shows a_{IP}, average acceleration between the 0.1 and 1 AU, as a function of V_{CME}.

3.3. An Alternative Approach: Fixed-Δt CMEs

The primary purpose of this study is to highlight issues with the current "spheroidal" implementations of cone-model CMEs in solar-wind models. However, we do outline a simple alternative approach here. It is not intended to be a complete solution to the problem; that will require careful calibration against observations in a future study.

For all spheroidal CMEs, the initial radial extent of the perturbation (and hence Δt), is determined by the CME angular width. Instead, we fix Δt at a constant value for all CMEs, regardless of CME speed or angular width. This means r_0 is now directly proportional to V_{CME}, consistent with faster CMEs expanding more, as observed (Owens et al., 2005). This fixed-Δt CME approach is simple to implement in current modeling frameworks (e.g., it required changing only a single line of code in HUXt, and is likely to be similarly straightforward for other solar-wind models): the shape and CME radial extent are computed in the exact same way as for the spheroidal CME, merely the speed at which the structure is advected through the inner boundary is altered to achieve the required Δt (though the speed of the perturbation at the solar-wind inner boundary remains V_{CME}).

For demonstration purposes, we use $\Delta t = 8$ hrs. The resulting relation between CME radial extent at 0.1 AU and V_{CME} is shown as the blue lines in Figures 3c and 3d. In Figure 3d, V_{1AU} is first converted to V_{CME} using the observed best-fit relation outlined above. In general, the model 0.1 AU radial extents are smaller than the 1 AU observations, consistent with continued CME expansion during propagation to Earth. But the same general trends are present.

Such fixed-Δt CMEs produce transversely elongated structures in the solar wind, as shown in Figures 2b and 2d, and consistent with expected distortion from spherical expansion (Owens et al., 2006; Riley & Crooker, 2004). Figure 2b shows some general illustrations: fixed-Δt CMEs of the same V_{CME} produce identical τ, regardless of angular width. They also produce the same ICME duration at 1 AU, regardless of angular width, as observed. Figure 2d suggests that these fixed-Δt CMEs produce τ more closely related to V_{CME} than spheroidal CMEs (i.e., there is no obvious plateau in τ at high V_{CME}). A trend between r_{1AU} and V_{CME} is also apparent, as observed.

Figure 6 shows the HUXt CME propagation results for the fixed-Δt CME approach. As illustrated in Figure 2b, CME kinematics are identical for all values of α. For slow CMEs ($V_{CME} \leq 400$ km s^{-1}), Δt is significantly smaller than for spheroidal CMEs, so the CME experiences more acceleration from the ambient solar wind. This produces lower τ values, reaching a maximum value of around 5 days, in much closer agreement with the observations. τ also continues to (non-linearly) decline with V_{CME} at high values, as suggested by the available observations. These lower τ values are achieved without a large systematic overestimation of V_{1AU} for slower and moderate CMEs. The net acceleration, a_{IP}, is still a little high for the fixed-Δt CMEs, but it is in far closer agreement with observations than wide spheroidal CMEs. Importantly, the a_{IP} trend with V_{CME} is the same for all values of α, as observed.

4. Summary and Discussion

Simple geometrical models—cone models—are routinely used with coronagraph observations to estimate the three-dimensional properties of CMEs near the Sun. In order to propagate these structures to Earth—for both research and space-weather forecasting purposes—a spherical (or spheroidal) perturbation is inserted at the inner boundary of a solar-wind model with the observed cone-model estimates of CME timing, direction, speed and angular width. The implicit assumption of the spheroidal CME approach is that the radial extent of the CME perturbation is related to the angular width of the CME. This study has examined the implications of that assumption.

Spheroidal CMEs produce a speed pulse at the solar-wind model inner boundary whose duration increases with CME angular width. The pulse duration, Δt, determines the degree to which the CME is affected by the ambient solar wind into which it propagates; lower Δt means a CME is more susceptible to solar-wind influence than greater Δt. By simulating different forms of spheroidal CMEs, with a range of different speeds and angular widths, and comparing with observed CME properties, we have shown:

1. Spheroidal CMEs have a radial extent at 0.1 AU, r_0, that increases with CME angular width. There is no evidence for this in the observations at 1 AU, although interplanetary dynamics between 0.1 and 1 AU could mask the effect.
2. Slow spheroidal CMEs produce very long Δt and thus are not accelerated up to the ambient solar wind speeds. This produces 1-AU transit times, τ, much longer than observed.
3. Spheroidal CMEs with moderate angular widths tend to overestimate τ for fast CMEs.
4. Spheroidal CMEs with large angular widths produce long Δt. While this is effective in producing the short τ values that are observed for the fastest CMEs, it greatly overestimates the ICME speed at 1 AU.
5. The interplanetary acceleration of CMEs between 0.1 and 1 AU shows significant disagreement with observations for very wide spheroidal CMEs.

We note that the results obtained in this study are based on a one-dimensional, reduced physics solar-wind model (HUXt). The expectation is that the same trends would be present regardless of solar-wind model used, as they are arise from purely geometric properties of cone CMEs. But future work will verify this.

While this study has focussed on speed perturbations to approximate CMEs, combined speed and density perturbations are also sometimes used (e.g., Odstrcil, Riley, & Zhao, 2004). This is unlikely to greatly affect the trends presented here, as both fast and slow CMEs become more resistant to acceleration by the ambient solar wind. These same issues will also be present in more sophisticated representations of CMEs, such as magnetic flux-ropes (Verbeke et al., 2019), if they are also approximated as spheroidal in shape. Evolving flux-rope approaches have been developed (Shiota & Kataoka, 2016), which can potentially alleviate these issues. However, for routine operational space-weather forecasting, these approaches are not practical, and the simple speed perturbations investigated here still need to be employed.

As an alternative to spheroidal CMEs we outlined a simple approach in which Δt is fixed, regardless of CME angular width or speed. This produces CMEs with r_0 that increases linearly with CME speed. This is in better agreement with the available observations both presented here, and with previous studies of ICME expansion at 1 AU (Owens et al., 2005). Using solar-wind modeling, we have shown that the fixed-Δt CME approach produces arrival times, arrival speeds and interplanetary accelerations that are in far better agreement with the available observations.

A somewhat arbitrary value of $\Delta t = 8$ hrs was used for demonstration purposes in this study. However, this value needs careful calibration against a large data set of combined CME (e.g., Kay & Palmerio, 2024) and ICME observations (e.g., Richardson & Cane, 2010), in order to find both the optimum value and its uncertainty range. The latter is required for accurate use in ensemble CME and solar-wind modeling (e.g., Edward-Inatimi et al., 2024; Mays et al., 2015; Owens & Riley, 2017). It may be possible that some speed or angular-width dependence of the Δt value is required, rather than being completely fixed. But these initial results suggest that any relation is likely to be small, and certainly significantly weaker than is introduced by the spheroidal CME approximation.

It will also be necessary to fully account for the uncertainty in the CME observations. The cone model parameters estimated from coronagraph observations are primarily estimated based on observations within 0.1 AU. The

speed and timing of the CME at 0.1 AU is then determined by simple ballistic extrapolation. As fast CMEs will decelerate most rapidly close to the Sun, owing to the slower ambient solar-wind speeds, this may introduce significant error into the initial CME conditions used in the solar-wind models.

The fixed-Δt CME approach presented here mimics CME expansion in terms of the duration of the CME perturbation at the inner boundary of the solar-wind model. But, as with spheroidal CMEs, the solar-wind speed is held constant at the coronagraph-derived speed, V_{CME}, as the CME passes through the inner boundary. That is, the time profile of the speed perturbation does not account for the expansion of the CME as it passes through the inner boundary, which would decline from the CME leading edge to the CME trailing edge. The effect on CME dynamics of introducing CMEs into solar-wind models with a declining speed profile, to be more consistent with expansion, will be investigated in a future study. However, quantifying CME expansion from observations is difficult, due to limited observations inside 1 AU and high event-to-event variability (Agarwal & Mishra, 2024; Savani et al., 2009). The simplicity of the cone-CME approach, in particular the lack of internal magnetic field structure, means that interpreting our results in terms of the physics of real CMEs is difficult. If these results are replicated in CME simulations using an internal flux-rope magnetic field (Verbeke et al., 2019), then we may be able to learn more about the dynamics of CMEs, particularly their radial expansion, close to the Sun.

Data Availability Statement

All code and data is available at Owens and Barnard (2025).

References

Agarwal, A., & Mishra, W. (2024). Non-conventional approach for deriving the radial sizes of coronal mass ejections at different instances: Discrepancies in the estimates between remote and in situ observations. *Monthly Notices of the Royal Astronomical Society*, *534*(3), 2458–2474. https://doi.org/10.1093/mnras/stae2260

Arge, C. N., Odstrcil, D., Pizzo, V. J., & Mayer, L. R. (2003). Improved method for specifying solar wind speed near the Sun. *AIP Conference Proceedings*, *679*(1), 190–193. https://doi.org/10.1063/1.1618574

Barnard, L., & Owens, M. (2022). HUXt—An open source, computationally efficient reduced-physics solar wind model, written in Python. *Frontiers in Physics*, *10*. https://doi.org/10.3389/fphy.2022.1005621

Brueckner, G. E., Howard, R. A., Koomen, M. J., Korendyke, C. M., Michels, D. J., Moses, J. D., et al. (1995). The Large Angle Spectroscopic Coronagraph (LASCO). *Solar Physics*, *162*(1), 357–402. https://doi.org/10.1007/BF00733434

Cargill, P. J. (2004). On the aerodynamic drag force acting on coronal mass ejections. *Solar Physics*, *221*(1), 135–149. https://doi.org/10.1023/B:SOLA.0000033366.10725.a2

Case, A. W., Spence, H. E., Owens, M. J., Riley, P., & Odstrcil, D. (2008). Ambient solar wind's effect on ICME transit times. *Geophysical Research Letters*, *35*(15), L15105. https://doi.org/10.1029/2008GL034493

Edward-Inatimi, N. O., Owens, M. J., Barnard, L., Turner, H., Marsh, M., Gonzi, S., et al. (2024). Adapting ensemble-calibration techniques to probabilistic solar-wind forecasting. *Space Weather*, *22*(12), e2024SW004164. https://doi.org/10.1029/2024SW004164

Emmons, D., Acebal, A., Pulkkinen, A., Taktakishvili, A., MacNeice, P., & Odstrcil, D. (2013). Ensemble forecasting of coronal mass ejections using the WSA-ENLIL with CONED Model. *Space Weather*, *11*(3), 95–106. https://doi.org/10.1002/swe.20019

Gopalswamy, N., Lara, A., Lepping, R. P., Kaiser, M. L., Berdichevsky, D., & St. Cyr, O. C. (2000). Interplanetary acceleration of coronal mass ejections. *Geophysical Research Letters*, *27*(2), 145–148. https://doi.org/10.1029/1999gl003639

Gopalswamy, N., Lara, A., Yashiro, S., Kaiser, M. L., & Howard, R. A. (2001). Predicting the 1-AU arrival times of coronal mass ejections. *Journal of Geophysical Research*, *106*(A12), 29207–29217. https://doi.org/10.1029/2001JA000177

Jin, M., Manchester, W. B., van der Holst, B., Sokolov, I., Tóth, G., Mullinix, R. E., et al. (2017). Data-constrained coronal mass ejections in a global magnetohydrodynamics model. *The Astrophysical Journal*, *834*(2), 173. https://doi.org/10.3847/1538-4357/834/2/173

Kay, C., & Palmerio, E. (2024). Collection, collation, and comparison of 3D coronal CME reconstructions. *Space Weather*, *22*(1), e2023SW003796. https://doi.org/10.1029/2023SW003796

Lee, C. O., Arge, C. N., Odstrcil, D., Millward, G., Pizzo, V., & Lugaz, N. (2015). Ensemble modeling of successive halo CMEs: A case study. *Solar Physics*, *290*(4), 1207–1229. https://doi.org/10.1007/s11207-015-0667-2

Lynch, B. J., Wyper, P. F., Palmerio, E., Casillas, L., Dahlin, J. T., Daldorff, L. K. S., et al. (2025). Synthetic remote-sensing and in situ observations of fine-scale structure in a pseudostreamer coronal mass ejection through the solar corona. *Astrophysical Journal Supplement*, *277*(2), 40. https://doi.org/10.3847/1538-4365/adb14e

Mays, M. L., Taktakishvili, A., Pulkkinen, A., MacNeice, P. J., Rastätter, L., Odstrcil, D., et al. (2015). Ensemble modeling of CMEs using the WSA–ENLIL+Cone model. *Solar Physics*, *290*(6), 1775–1814. https://doi.org/10.1007/s11207-015-0692-1

Merkin, V. G., Lyon, J. G., Lario, D., Arge, C. N., & Henney, C. J. (2016). Time-dependent magnetohydrodynamic simulations of the inner heliosphere. *Journal of Geophysical Research*, *121*(4), 2866–2890. https://doi.org/10.1002/2015JA022200

Michalek, G., Gopalswamy, N., & Yashiro, S. (2003). A new method for estimating widths, velocities, and source location of halo coronal mass ejections. *The Astrophysical Journal*, *584*(1), 472–478. https://doi.org/10.1086/345526

Odstrcil, D., Pizzo, V., Linker, J. A., Riley, P., Lionello, R., & Mikic, Z. (2004). Initial coupling of coronal and heliospheric numerical magnetohydrodynamic codes. *Journal of Atmospheric and Solar-Terrestrial Physics*, *66*(15–16), 1311–1320. https://doi.org/10.1016/j.jastp.2004.04.007

Odstrcil, D., Riley, P., & Zhao, X.-P. (2004). Numerical simulation of the 12 May 1997 interplanetary CME event. *Journal of Geophysical Research*, *109*(A2). https://doi.org/10.1029/2003JA010135

Owens, M., & Barnard, L. (2025). Code and data for implications of using spheroidal CMEs in solar-wind models [Software]. *Zenodo*. https://doi.org/10.5281/zenodo.15121472

Owens, M., Lang, M., Barnard, L., Riley, P., Ben-Nun, M., Scott, C. J., et al. (2020). A computationally efficient, time-dependent model of the solar wind for use as a surrogate to three-dimensional numerical magnetohy drodynamic simulations. *Solar Physics*, *295*(3), 43. https://doi.org/10.1007/s11207-020-01605-3

Owens, M. J., & Cargill, P. J. (2004). Predictions of the arrival time of Coronal Mass Ejections at 1 AU: An analysis of the causes of errors. *Annals of Geophysics*, *22*(2), 661–671. https://doi.org/10.5194/angeo-22-661-2004

Owens, M. J., Cargill, P. J., Pagel, C., Siscoe, G. L., & Crooker, N. U. (2005). Characteristic magnetic field and speed properties of interplanetary coronal mass ejections and their sheath regions. *Journal of Geophysical Research*, *110*(A1), 1–9. https://doi.org/10.1029/2004JA010814

Owens, M. J., Lockwood, M., & Barnard, L. A. (2020). The value of CME arrival time forecasts for space weather mitigation. *Space Weather*, *18*(9), e2020SW002507. https://doi.org/10.1029/2020SW002507

Owens, M. J., Merkin, V. G., & Riley, P. (2006). A kinematically distorted flux rope model for magnetic clouds. *Journal of Geophysical Research*, *111*(A3), A03104. https://doi.org/10.1029/2005JA011460

Owens, M. J., & Riley, P. (2017). Probabilistic solar wind forecasting using large ensembles of near-Sun conditions with a simple one-dimensional "Upwind" scheme. *Space Weather*, *15*(11), 1461–1474. https://doi.org/10.1002/2017SW001679

Pomoell, J., & Poedts, S. (2018). EUHFORIA: European heliospheric forecasting information asset. *Journal Space Weather Space Climate*, *8*, A35. https://doi.org/10.1051/swsc/2018020

Richardson, I. G., & Cane, H. V. (2010). Near-earth interplanetary coronal mass ejections during solar cycle 23 (1996–2009): Catalog and summary of properties. *Solar Physics*, *264*(1), 189–237. https://doi.org/10.1007/s11207-010-9568-6

Riley, P., & Crooker, N. U. (2004). Kinematic treatment of CME evolution in the solar wind. *The Astrophysical Journal*, *600*(2), 1035–1042. https://doi.org/10.1086/379974

Riley, P., Linker, J. A., & Mikic, Z. (2001). An empirically-driven global MHD model of the solar corona and inner heliosphere. *Journal of Geophysical Research*, *106*, 15889–15902. https://doi.org/10.1029/2000JA000121

Riley, P., & Lionello, R. (2011). Mapping solar wind streams from the Sun to 1 AU: A comparison of techniques. *Solar Physics*, *270*(2), 575–592. https://doi.org/10.1007/s11207-011-9766-x

Riley, P., Mays, L., Andries, J., Amerstorfer, T., Biesecker A, D., Delouille, V., et al. (2018). Forecasting the arrival time of coronal mass ejections: Analysis of the CCMC CME scoreboard. *Space Weather*, *16*(9), 1245–1260. https://doi.org/10.1029/2018SW001962

Savani, N., Rouillard, A. P., Davies, J. A., Owens, M. J., Forsyth, R. J., Davis, C. J., & Harrison, R. A. (2009). The radial width of a coronal mass ejection between 0.1 and 0.4 AU estimated from the heliospheric imager on STEREO. *Annals of Geophysics*, *27*(11), 4349–4358. https://doi.org/10.5194/angeo-27-4349-2009

Scolini, C., & Palmerio, E. (2024). The spheroid CME model in EUHFORIA. *Journal Space Weather Space Climate*, *14*, 13. https://doi.org/10.1051/swsc/2024011

Scolini, C., Verbeke, C., Poedts, S., Chané, E., Pomoell, J., & Zuccarello, F. P. (2018). Effect of the initial shape of coronal mass ejections on 3-D MHD simulations and Geoeffectiveness predictions. *Space Weather*, *16*(6), 754–771. https://doi.org/10.1029/2018SW001806

Shiota, D., & Kataoka, R. (2016). Magnetohy drodynamic simulation of interplanetary propagation of multiple coronal mass ejections with internal magnetic flux rope (SUSANOO-CME). *Space Weather*, *14*(2), 56–75. https://doi.org/10.1002/2015SW001308

Temmer, M., Holzknecht, L., Dumbović, M., Vršnak, B., Sachdeva, N., Heinemann, S. G., et al. (2021). Deriving CME density from remote sensing data and comparison to in situ measurements. *Journal of Geophysical Research*, *126*(1), e2020JA028380. https://doi.org/10.1029/2020JA028380

Temmer, M., Scolini, C., Richardson, I. G., Heinemann, S. G., Paouris, E., Vourlidas, A., et al. (2023). CME propagation through the heliosphere: Status and future of observations and model development. *Advances in Space Research*. https://doi.org/10.1016/j.asr.2023.07.003

Thernisien, A., Vourlidas, A., & Howard, R. A. (2009). Forward modeling of coronal mass ejections using STEREO/SECCHI data. *Solar Physics*, *256*(1–2), 111–130. https://doi.org/10.1007/s11207-009-9346-5

Torok, T., Downs, C., Linker, J. A., Lionello, R., Titov, V. S., Mikić, Z., et al. (2018). Sun-to-Earth MHD simulation of the 2000 July 14 "Bastille Day". *Eruption. Astrophys. Journal.*, *856*(1), 75. https://doi.org/10.3847/1538-4357/aab36d

Toth, G., Sokolov, I. V., Gombosi, T. I., Chesney, D. R., Clauer, C. R., De Zeeuw, D. L., et al. (2005). Space weather modeling framework: A new tool for the space science community. *Journal of Geophysical Research*, *110*(A12), A12226. https://doi.org/10.1029/2005JA011126

van der Holst, B., Sokolov, I. V., Meng, X., Jin, M. W. B., Manchester, I., Tóth, G., & Gombosi, T. I. (2014). Alfvén Wave Solar Model (AWSoM): Coronal heating. *The Astrophysical Journal*, *782*(2), 81. https://doi.org/10.1088/0004-637X/782/2/81

Verbeke, C., Pomoell, J., & Poedts, S. (2019). The evolution of coronal mass ejections in the inner heliosphere: Implementing the spheromak model with EUHFORIA. *Astronomy and Astrophysics*, *627*, A111. https://doi.org/10.1051/0004-6361/201834702

Vrsnak, B., & Gopalswamy, N. (2002). Influence of aerodynamic drag on the motion of interplanetary ejecta. *Journal of Geophysical Research*, *107*(2), 1019. https://doi.org/10.1029/2001JA000120

Wu, C.-C., Liou, K., Wood, B. E., & Hutting, L. (2024). Effects of background solar wind and drag force on the propagation of coronal-mass-ejection-driven shocks. *The Astrophysical Journal*, *977*(2), 212. https://doi.org/10.3847/1538-4357/ad88ee

Zhao, X.-P., Plunkett, S. P., & Liu, W. (2002). Determination of geometrical and kinematical properties of halo coronal mass ejections using the cone model. *Journal of Geophysical Research*, *107*(A8). https://doi.org/10.1029/2001JA009143